

## Broadband, monochromatic and quasi-monochromatic x-ray propagation in multi-Z media for imaging and diagnostics

This content has been downloaded from IOPscience. Please scroll down to see the full text.

2017 Phys. Med. Biol. 62 6361

(<http://iopscience.iop.org/0031-9155/62/16/6361>)

View [the table of contents for this issue](#), or go to the [journal homepage](#) for more

Download details:

IP Address: 140.254.78.46

This content was downloaded on 20/07/2017 at 17:52

Please note that [terms and conditions apply](#).

6th myQA release now available

**myQA** ENLIGHTENING YOUR QA WORLD

All your QA applications & data integrated into one central platform.

All-in-One.  
All Connected.  
All Secure.

Iba

[be-dosimetry.com](http://be-dosimetry.com)

# Broadband, monochromatic and quasi-monochromatic x-ray propagation in multi-Z media for imaging and diagnostics

Maximillian S Westphal<sup>1</sup>, Sara N Lim<sup>1,6</sup>, Sultana N Nahar<sup>2</sup>,  
Enam Chowdhury<sup>4,5</sup> and Anil K Pradhan<sup>1,2,3</sup>

<sup>1</sup> Biophysics Graduate Program, The Ohio State University, Columbus, OH 43210, United States of America

<sup>2</sup> Department of Astronomy, The Ohio State University, Columbus, OH 43210, United States of America

<sup>3</sup> Chemical Physics Program, Department of Chemistry, The Ohio State University, Columbus, OH 43210, United States of America

<sup>4</sup> Department of Physics, The Ohio State University, Columbus, OH 43210, United States of America

<sup>5</sup> Department of Material Science and Engineering, The Ohio State University, Columbus, OH 43210, United States of America

E-mail: [pradhan.1@osu.edu](mailto:pradhan.1@osu.edu) and [westphal.21@osu.edu](mailto:westphal.21@osu.edu)

Received 3 January 2017, revised 14 June 2017

Accepted for publication 30 June 2017

Published 20 July 2017



CrossMark

## Abstract

With the advent of monochromatic and quasi-monochromatic x-ray sources, we explore their potential with computational and experimental studies on propagation through a combination of low and high-Z (atomic number) media for applications to imaging and detection. The multi-purpose code GEANT4 and a new code PHOTX are employed in numerical simulations, and a variety of x-ray sources are considered: conventional broadband devices with well-known spectra, quasi-monochromatic laser driven sources, and monochromatic synchrotron x-rays. Phantom samples consisting of layers of low-Z and high-Z material are utilized, with atomic-molecular species ranging from H<sub>2</sub>O to gold. Differential and total attenuation of x-ray fluxes from the different x-ray sources are illustrated through simulated x-ray images. Main conclusions of this study are: I. It is shown that a 65 keV Gaussian quasi-monochromatic source is capable of better contrast with less radiation exposure than a common 120 kV broadband simulator. II. A quantitative measure is defined and computed as a metric to compare the efficacy of any two x-ray sources, as a function of concentration of high-Z moieties in

<sup>6</sup>Now at: Medical College of Wisconsin, Milwaukee WI, United States of America

predominantly low- $Z$  environment and depth of penetration. III. Characteristic spectral features of  $K\alpha$ ,  $K\beta$  fluorescent emission and Compton scattering indicate pathways for accelerating x-ray photoexcitation and absorption; in particular, we model the tungsten  $K\alpha$  at 59 keV alongside experimental measurements at the European synchrotron research facility to search for the signature of induced  $K\alpha$  resonance fluorescence. The present study should contribute to the understanding of diagnostic potential of new x-ray sources under development, as well as the underlying fundamental physical processes and features for biomedical applications.

Keywords: x-ray devices, x-ray imaging, monochromatic x-ray, quasi-monochromatic x-ray, GEANT4, resonance fluorescence

(Some figures may appear in colour only in the online journal)

## 1. Introduction

In recent years a variety of x-ray sources have been under development. Spectroscopically, they can generally be classified as conventional broadband x-rays (BX), quasi-monochromatic x-rays (QX), and monochromatic x-rays (MX) sources (e.g. Le Sech *et al* (2000) and Hoheisel *et al* (2005)). Whereas the BX sources used in medical imaging and therapy are the most familiar, and MX produced by sources such as synchrotrons are also well studied, the QX sources are relatively new and offer potential advantages over BX and MX (Powers *et al* 2014, Khrennikov *et al* 2015). But primarily they produce BX bremsstrahlung spectra that is continuous across a wide energy range up to the maximum potential between the cathode and the anode. Sources that seek to modulate the continuum with more specificity have been in use in mammography (Birch *et al* 2006). The problems with BX spectra are well known and include: low energy x-ray absorption by intervening body tissue and photon scattering. To circumvent these problems and to attain greater efficiency, new x-ray sources are under development that can be targeted near-monochromatically for specific purposes according to the recipient entity.

Among the advantages of monochromatic sources is that, given the dominant source energy or range and targeted moieties, the propagation of radiation may be modelled *a priori* according to depth, concentration, etc for more precise dosimetry (Hoheisel *et al* 2005, Pradhan *et al* 2009, Montenegro *et al* 2009). To begin with, the cross sections for x-ray scattering and absorption, as well as the nature of the physical processes that determine their interactions, are relatively well-known. However, monochromatic sources may also trigger new physical effects that require more detailed studies than hitherto. A variety of phenomena, observed experimentally and explored theoretically are of interest. These relate to complex atomic physics and plasma physics that comes into play when monochromatic x-rays activate deep inner-shell excitations, especially related to  $K$ - and  $L$ -shell absorption and emission spectra. While these myriad phenomena are generally regarded as Auger processes, their manifestation in a particular environment is highly dependent of x-ray energy and intensity of the source.

One may divide x-ray sources into three groups. The first group consists of broadband radiation across a range of x-ray energies produced by bremsstrahlung radiation resulting from accelerated electrons striking a high- $Z$  target such as tungsten ( $Z = 74$ ). The second type, QX sources, are selective in terms of energy with relatively low background. The QX may be obtained through Bragg reflection at specified wavelengths employing the mosaic HOPG (highly oriented pyrolytic graphite) crystal, and have been modelled for imaging applications (e.g. Baldelli *et al* (2003) and Hoheisel *et al* (2005)). In recent years, there has been

considerable progress on generating QX using high-intensity lasers. The most straightforward way is laser-driven acceleration of electrons to relativistic velocities in a high- $Z$  target (Storm *et al* 2014). The resultant spectra are dominated by the  $K\alpha(Z)$  line, and a background that is considerably less pronounced than the BX sources.

Even more remarkably, tunable QX in the keV to MeV range can now be generated via inverse Compton scattering with laser-wakefield accelerated electrons using a single terawatt high-intensity laser (Achterhold *et al* 2013, Chen *et al* 2013, Powers *et al* 2014, Khrennikov *et al* 2015, Banerjee *et al* 2015); the resultant QX spectra are peaked around a central energy and may be characterized in terms of a full-width-half-maximum. The third type of sources are synchrotrons that generate MX, but they are not ideally suited for imaging owing to their high intensities, size and cost. However, a compact laser-driven x-ray source has been developed recently employing inverse Compton scattering between a high-intensity laser and an electron beam from a storage ring (Achterhold *et al* 2013).

Owing to the development of such narrow-band x-ray sources, the primary aim is to model and compare BX, QX, and MX spectra with respect to imaging and other applications. The crucial quantities that determine the propagation of radiation and efficacy are the spectral distribution of the source and the physical atomic-molecular properties of the target. The interaction of radiation with matter is energy-dependent owing to differential photon absorption and scattering by varied constituents in a given medium. The propagation and resultant attenuation of monochromatic or quasi-monochromatic X/ $\gamma$ -rays through biological material and other light-mid elements has been studied previously (Storm *et al* 2014) to quantify the mechanism of attenuation of x-rays propagating through various media, especially in material interspersed with high- $Z$  contrast agents (Cho 2005, Leung *et al* 2011).

The secondary aim is to carry out another set of simulations to theoretically study physical processes such as the atomic Auger effect and  $K\alpha$  resonance fluorescence that may enhance monochromatic x-ray absorption for biomedical applications. In earlier works,  $K\alpha$  resonant excitations have been predicted and observed (Nahar *et al* 2011). Resonance positions and strengths in high- $Z$  atomic systems such as iron and gold were calculated (Pradhan *et al* 2009, Montenegro *et al* 2009), and observed experimentally using intense x-ray free-electron laser (XFEL) in a warm dense aluminum plasma (Vinko *et al* 2012). In particular, we have suggested a mechanism that could, in principle, accelerate x-ray absorption via the Auger decay cycle through a twin-beam x-ray photoexcitations tuned to the  $K$ -edge and the characteristic  $K\alpha$  transition energy (Nahar and Pradhan 2015). We describe an experiment and simulation on the European synchrotron research facility (ESRF) to search for signal of  $K\alpha$  resonance fluorescence in tungsten. We have modelled these ESRF experiments using GEANT4 (Agostinelli *et al* 2003, Allison *et al* 2006, 2016), an open-source toolkit developed by CERN that uses the Monte Carlo method to simulate the passage of particles through matter. These simulations of the observed ESRF spectra show clear correlations but also point to missing physics and physical processes that might manifest themselves, or may be implemented with new MX or QX sources. For example, related processes such as nuclear resonance fluorescence are not incorporated in the base source code of GEANT4 and have been developed by other groups (Lakshmanan *et al* 2014). We discuss the prospects of novel experimental and theoretical methodologies that might enable low energy x-rays to be utilized efficiently in medical research using high- $Z$  moieties.

## 2. Theoretical considerations

In this section we outline the theoretical quantities that underpin numerical models of x-ray sources and their interactions with high- $Z$  elements.

## 2.1. Spectral distributions and cross sections

Broadband x-ray sources are essentially the original Roentgen tube with a bremsstrahlung output spectrum. In contrast, emerging QX and MX sources are highly complex, such as those based on high-intensity lasers and electron accelerators. Figure 1 shows BX, QX and MX spectra produced by a variety of sources considered in this study.

The 40kV and 120kV BX sources in figures 1(a) and (b) are typical of those employed in medical imaging, for example 120kV CT scanners also show the tungsten  $K\alpha$  at  $\sim 60$ keV. On the other hand, the QX sources span a wide range and may be produced through several devices. All QX sources have a high-intensity laser in common, although its implementation varies. A high-intensity laser striking a high-Z target, such as zirconium with  $K\alpha$  15.7keV and silver with  $K\alpha$  of 22.0keV, accelerates electrons to relativistic velocities which then emit bremsstrahlung output spectra dominated by the said  $K\alpha$ ,  $K\beta$  of the target atom as shown in figures 1(c) and (d) respectively. These dominant peaks become the effective energy of that source. While the output from the high-intensity laser striking a high-Z target produces a lower x-ray background than the BX sources, a disadvantage is apparent from figures 1(c) and (d); their output is dominated by relatively large low-energy flux that would render them unsuitable for imaging applications without filters that would then reduce the available overall intensity. Another type of QX spectra may be obtained with a BX source striking a high-Z target, such as a 150kV x-ray source with a zirconium target shown in figure 1(e); the spectrum is again dominated by the  $K\alpha$ ,  $K\beta$  and with lower background than BX, but the fluxes obtained are quite low; this has been termed broadband-to-monochromatic conversion (B2MX) spectra (Lim *et al* 2015). QX spectra are also produced from Bragg diffraction using a mosaic crystal (*viz.* HOPG), according to the Bragg relation  $n\lambda = 2d \sin \theta_B$ ; characteristic Bragg angles  $\theta_B$  produce fairly Gaussian shaped QX output spectra centered around  $\lambda$  characteristic of the crystal lattice spacing  $d$  (Baldelli *et al* 2003). The most advanced and promising QX sources are laser driven but also combined with high-energy electron accelerators. Inverse Compton scattering with relativistic electron beams upscatters the laser photon energy to x-rays in the keV-MeV range (Achterhold *et al* 2013, Chen *et al* 2013, Powers *et al* 2014, Khrennikov *et al* 2015, Banerjee *et al* 2015). As with the Bragg scattered QX, the output spectral shape is also approximately Gaussian and may be modelled as shown in figure 1(f), where the spectral linewidth is chosen based on data shown in Powers *et al* (2014). Finally, the highly monochromatic sources are the synchrotrons tuned to produce MX spectra at various energies shown in figure 1(g). The 60keV MX spectrum was chosen to emulate an idealized 120kV CT scan. The 20keV MX spectrum was chosen because it is similar energy to both the zirconium  $K\alpha$  and silver  $K\alpha$ . The 40keV MX spectrum was chosen as a midpoint between the two previously mentioned MX sources in addition to being the maximum possible energy of the BX 40kV source.

## 2.2. Differential x-ray attenuation

We may write the general expression for attenuation of x-ray intensity for our case as

$$I_E = I_o \exp(-\kappa_E \rho x), \quad (1)$$

where  $I_E$  is the x-ray flux at energy  $E$ ,  $x$  is the depth of penetration along the incident direction,  $I_o$  the flux at a depth  $x = 0$ ,  $\kappa_E$  is the attenuation coefficient ( $\text{cm}^2 \text{g}^{-1}$ ),  $\rho$  is the density of a combination of water and some sensitizer concentration  $\epsilon$  (e.g.  $\text{mg ml}^{-1}$ ). In addition to the four variables explicit in equation (1), the flux at any energy is implicitly dependent on the bremsstrahlung distribution  $F_{\text{BX}}(V, E)$ , where we denote the maximum voltage of the

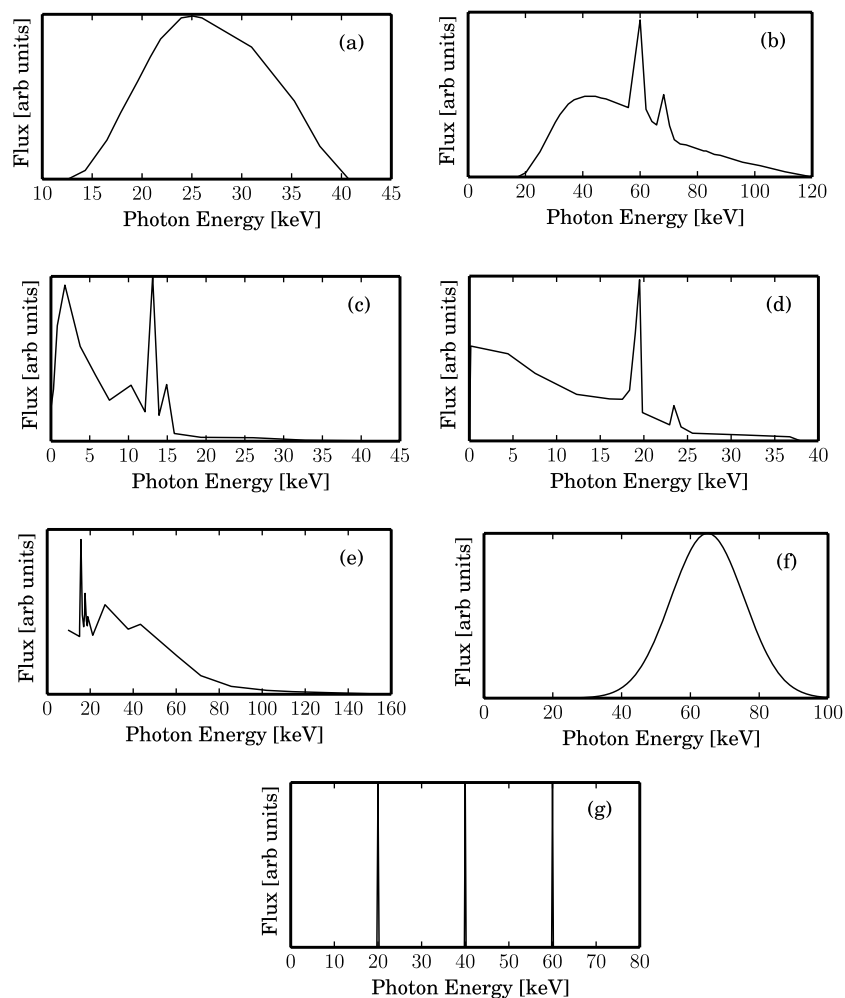


**Figure 1.** The eight spectra used in GEANT4 simulations—two broadband (BX), three quasi-monochromatic (QX), and three monochromatic (MX): (a) BX 40kV, (b) BX 120kV with tungsten target (CT Scan); (c) QX high-intensity laser with zirconium target with  $K\alpha$  15.7 keV, and (d) silver target with  $K\alpha$  22.0 keV; (e) QX broadband-to-monochromatic x-ray (B2MX) conversion of 150kV source using zirconium target; (f) QX inverse Compton scattering; (g) MX 20, 40, 60 keV.

x-ray source by  $V$ . In addition, we may further sub-divide  $\kappa_E$  between photoexcitation (PE) of target atoms as  $\kappa_E(\text{PE})$ , and isolating the PE component from the total attenuation coefficient as  $\kappa_E(\text{Tot})$ , where the other largest component is due to incoherent Compton scattering (Lim *et al* 2015). Thus, x-ray intensity attenuation may be computed for both cases to elucidate the nature of PE absorption alone. Given a spectral distribution  $F_{\text{BX}}(V)$ , the integrated intensity attenuation up to a depth  $D(\text{cm})$  is

$$I(D, V) = \int_0^D \int_{E_i}^{E_V} F_{\text{BX}}(V, E) \exp(-\kappa_E \rho x) dx dE, \quad (2)$$

where  $E_i$  is the truncated lower limit of the filtered bremsstrahlung energy distribution (viz. figure 1) and  $E_V$  is the maximum energy given the maximum voltage of the x-ray source  $V$ .

Equation (2) needs to be qualified to account for the variation of  $\kappa_E$  in a multi-media environment, such as in the presence of a high- $Z$  sensitizer in water of combined density  $\rho$  at depth  $d$ . Equation (2) can now be used to study variation of the *differential attenuation* of incident x-ray intensity  $I$  with respect to depth  $d$ , and a concentration factor  $\epsilon$ . For example, we consider a water phantom embedded with a layer of radiosensitizing agent  $Z$  at a given depth  $d$ , energy  $E$ , total concentration  $\rho_{\epsilon Z + H_2O}$ , and coefficient  $\kappa_E(\epsilon\rho_Z + \rho_{H_2O})$ , where  $\epsilon$  is the fractional concentration expressed as  $\text{mg ml}^{-1}$  (e.g.  $\epsilon = 0.001$  or  $1 \text{ mg ml}^{-1}$ ). The variation of  $I$  versus  $x$  between two successive depths  $x_i$  and  $x_{i+1}$  then written as

$$\frac{\delta I}{I_o} = \frac{I_{x_i}(\rho_{(\epsilon Z + H_2O)}) - I_{x_{i+1}}(\rho_{(\epsilon Z + H_2O)})}{I_o}. \quad (3)$$

Equation (3) is evaluated for the entire phantom with a sensitized layer at depth  $d$  and fixed sensitizer concentration  $\epsilon$ . We emphasize that this expression may be evaluated using equation (2) using either the PE coefficients alone, responsible for the production of Auger electrons, or the total incident radiation dose including Compton scattering.

We can also compare the differential intensity versus  $\epsilon$ , at a fixed depth  $d$  and varying the concentration factor  $\epsilon$ , relative to  $H_2O$  alone, as

$$\frac{\delta I_x[\rho_{(\epsilon Z + H_2O)}]}{\delta I_x[\rho_{(H_2O)}]} = \frac{I_{x_i}[\rho_{(\epsilon Z + H_2O)}] - I_{x_{i+1}}[\rho_{(\epsilon Z + H_2O)}]}{I_{x_i}[\rho_{(H_2O)}] - I_{x_{i+1}}[\rho_{(H_2O)}]}. \quad (4)$$

Now we can make a quantitative comparison of two different x-ray sources with maximum potential  $V$  and  $V'$  by defining the *radiosensitization ratio* (RR). Moreover, the RR is also expressed so as to measure the change in attenuation with respect to intensity at different sensitizer concentrations, say  $\rho_1$  and  $\rho_2$ , i.e.

$$\eta(V, V'; \rho_1, \rho_2) = \frac{[I(\rho_2) - I(\rho_1)]_V}{[I(\rho_2) - I(\rho_1)]_{V'}}, \quad (5)$$

where the intensity  $I$  is computed as in equation (2). The main point is that the RR ratio  $\eta$  in equation (5) can be calculated for PE and total absorption separately,  $\eta_P$  and  $\eta_T$ , for any two x-ray sources to reveal the effect of Auger ionization from PE alone relative to total, and also as function of the sensitizer concentration, e.g.  $\rho_1 = \rho_{(\epsilon_1 Z + H_2O)}$  that quantifies high- $Z$  concentration in water.

### 3. Materials and methods

Numerical simulations with the aim of describing empirical environments are carried out using simplified phantoms and high- $Z$  materials acting as sensitizing or contrast agents. x-ray propagation is modelled with codes taking account of known physical processes as well as novel mechanisms that might be activated using new x-ray sources for imaging and other applications.

#### 3.1. Computational formalism

The computations are carried out using a new modelling code PHOTX with respect to variables that determine x-ray absorption leading to high- $Z$  sensitization. In order to compute the quantities derived from equations (2)–(5), we implement an algorithm based on the formalism outlined in the previous section into PHOTX (a Fortran computer program). Owing to the number of dependent variables involved in simulations based on equations ((1)–(4)),—energy,

depth, concentration, attenuation coefficients, spectral distributions, and differentiation of photoelectric component relative to total absorption. The input data to PHOTX includes the detailed bremsstrahlung distributions  $F_{BB}(V, E)$  shown in figure 1 and in equation (2), and attenuation coefficients  $\kappa_{PE}(E)$  and  $\kappa_{Tot}(E)$  for photoabsorption and total absorption (including Compton scattering), respectively.

### 3.2. GEANT4 Monte Carlo simulations

GEANT4 is a general purpose open software package that enables Monte Carlo simulations of energy-particle interactions in different media in a pre-specified environment or *phantom*. We consider a relatively simple overall biological environment consisting of water and an embedded layer sensitized with an high-Z agent at certain depth. However, the complexity of the calculations manifests itself when all relevant processes and ranges of variables are included, as described above. Simulations in GEANT4 were carried out using version 10.01 and the ‘G4EmPenelope physics list’.

**3.2.1. Phantom environments.** In order to simplify the otherwise complex environments in practice, we introduce two types of phantoms, one rectangular and the other spherical. In addition, layers or sub-shells are included to simulate x-ray propagation through multi-Z media. Figures 2(a) and (b) schematically illustrate the two phantoms, illuminated by x-ray source(s) considered herein. For x-ray imaging we assume three different 1 cm layers of air, water and bone, distributed across a 5 cm total span of water in the rectangular phantom in figure 2(a). The spherical phantom in figure 2(b) is a 2.5 cm radius sphere of water containing a 1 cm radius sub-sphere of air, water, and bone. The phantoms are irradiated by the individual x-ray source(s) shown in figure 1, and normalized photon absorption counts obtained from GEANT4. Total x-ray absorption is converted to a contrast image, simulating exposure on an ordinary x-ray film. In this particular manner, we can also qualitatively compare and contrast input and output numerical data pertaining to each x-ray source vis-a-vis imaging applications.

The spherical phantom is divided into rectangular segments of length  $h = 0.1$  cm along the radius  $R$  with length  $a = \sqrt{R^2 - (R - h)^2}$ , the distance to outside of sphere. For each source, only the portions of the sphere including the inner sub-sphere were simulated because the pure water edges of spheres were identical with changing sub-sphere.

**3.2.2. Input spectra and x-ray attenuation.** The method requires each digital spectral shape as input to GEANT4. For the quasi-monochromatic sources, experimentally obtained spectra are used to characterize the input beam while broadband spectra were directly measured from various in-house sources. Photon counts of each spectrum are computed and normalized to allow a pseudo random number generator to approximate the shape using GEANT4’s particle gun mode. Each simulation consisted of 10 million photons to create an accurate representation of the spectra. The number of photons arriving at the detector, represented in simulations as a thick slab of lead, were then analysed.

### 3.3. Absorption efficiency metric

In order to facilitate quantitative analysis comparing diverse x-ray sources with diverse spectral profiles, another code, PHOTX, has been written to analyse x-ray absorption through a phantom with embedded high-Z element layer(s). The purpose is more specific than the general modeling in GEANT4. PHOTX separates out the photon scattering component from the

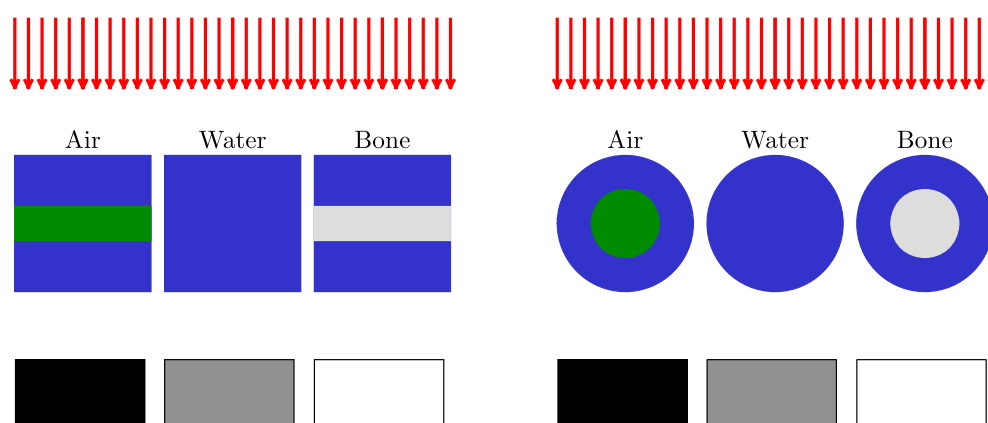


**Figure 2.** Air—green, water—blue, bone—white, x-rays—red. Grayscale rectangles show number of photons reaching the detector, with darker representing more photons. Left: Rectangular phantom: representation of multi-layered phantom setup in GEANT4 for simulation of chest x-ray imaging. Phantom was 2 cm of water, 1 cm of either air, water, or bone, and 2 cm of water. Right: Representation of the spherical phantom used in GEANT4. Phantom was a 2.5 cm radius sphere of water surrounding a 1.0 cm radius sub-sphere of either air, water, or bone.

photoexcitation component, the latter corresponds to direct absorption and ionization by inner electronic shells. Low energy x-rays, below 100 keV, predominantly influence photoexcitation, whereas high energy MeV x-rays mainly result in Compton scattering (Lim *et al* 2015). The quantity  $\eta$  defined in section 2.2 is a metric that is computed by PHOTX for any two sources and specified high- $Z$  sensitizer concentration and depth. In order to compare x-rays from low energy versus high energy BX sources by a common high- $Z$  sensitizer, such as carboplatin or cisplatin, we employ a linear water phantom of 15 cm depth with an embedded 1 cm layer of gold of varying concentrations at a depth of 10 cm. PHOTX calculations are then carried out for 3 low energy BX sources with 100 kV, 160 kV and 250 kV, compared with a typical high energy 6 MV LINAC (Lim *et al* 2015). In addition to the sources detailed in previous sections, a variety of low-energy sources were chosen as a more general study of absorption of low energy versus high energy x-ray sources. The main reason is that low-energy spectral profiles vary much more rapidly with x-ray energy than the relatively flat high-energy MV source output (Lim *et al* 2015). The results presented cover most of the keV energy range from common low-energy BX sources, compared to a high-energy MV source producing MeV x-rays.

### 3.4. Synchrotron experiment

In order to detect possible signature of  $K\alpha$  resonance fluorescence mentioned earlier with reference to earlier theoretical and experimental studies (Pradhan *et al* 2009, Montenegro *et al* 2009, Nahar and Pradhan 2015, Vinko *et al* 2012), we conducted an experiment at ESRF on beamline ID17 using an x-ray beam aligned with a Si-bent Laue crystal to filter out unwanted energies and focused to a  $5 \text{ mm} \times 5 \text{ mm}$  area. This beam was tuned to vary in the energy range spanning around and in between the  $K\alpha$  and  $K\beta$  transitions with a tungsten target. A X-123 Cd-Te with 4 mm Be window detector from Amptek was calibrated using a  $^{241}\text{Am}$  radioactive source, with a resulting error of  $\pm 700 \text{ eV}$  in calibration and a detection efficiency of 90% or higher for the energies of interest (Redus *et al* 2006). The detector was placed at

two angles, 40° and 140° degrees, relative to the incident photon beam to obtain output spectra in the both the forward and backward scattering directions. Target used was a 230  $\mu\text{m}$  thick tungsten plate set perpendicular to the beam. The transverse area of the tungsten plate is larger than the beam area listed above. The x-ray flux on the target was proportional to the current in the storage ring, so we normalized the results by dividing detected counts by the measured current for each experiment. The experimental schematic is shown in figure 9.

## 4. Results and discussion

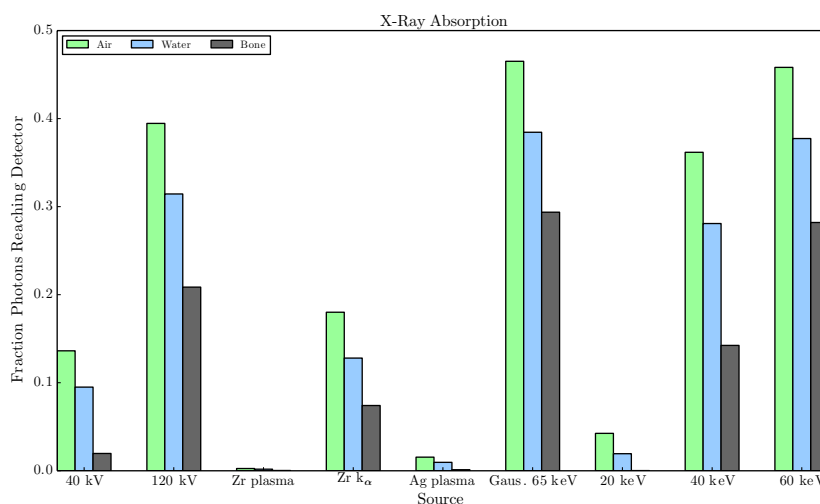
We describe the results of GEANT4 calculations for all types of x-ray sources considered with respect to the rectangular and spherical phantoms described in the previous section, consisting of water, air and bone layers. Photon absorption counts obtained from GEANT4 are converted to corresponding simulated images, with contrast level as indicator of amount of absorption versus x-ray exposure for normalized radiation input. The main focus of these studies is on the new QX and MX sources that are in the low energy region,  $E < 100$  keV, which is also the energy region where high-Z atomic species may effectively act as contrast agents owing to x-ray absorption by inner electronic shells. In addition, we demonstrate the use of the metric  $\eta$  for evaluating the absorption efficiency of two x-ray sources using the code PHOTX to compare high energy MV linear accelerator (LINAC) input spectra as opposed to low energy kV fluxes.

### 4.1. X-ray absorption and imaging

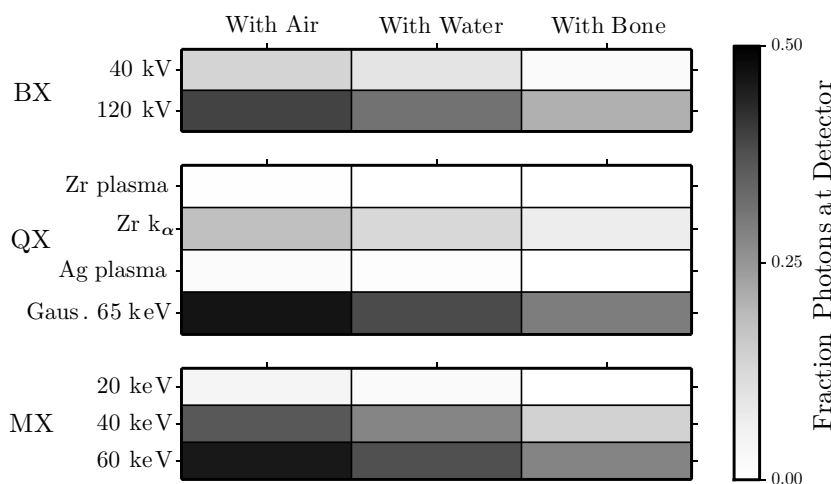
Figure 3 shows photon counts detected through each of the air, water and bone layers for all x-ray sources in the rectangular phantom. Approximately, the results may be divided according to high, low and medium absorption counts. x-rays from high-intensity laser generated Zr-plasma and Ag-plasma are nearly totally absorbed, as their fluxes are dominated by very low energies. Zr- $K\alpha$  at 16 keV and Ag- $K\alpha$  at 22 keV (figure 1). Similarly, the filtered Zr- $K\alpha$  and the monochromatic 20 keV photons are unable to substantially penetrate the phantom. On the other hand, and as expected, relatively low absorption is found from BX 120 kV, QX 65 keV (modelled as a Gaussian), and MX 60 keV, which show significant penetration through the layers with much higher number of photons reaching the detector or imaging device. Medium absorption of photons is observed from the 40 kV BX and the filtered Zr- $K\alpha$  that lie in between the previously discussed absorption regimes.

Figure 4 represents the transformation of the GEANT4 absorption counts through various layers, and the combination, on to color-contrast images, as simulation of x-ray exposure on a film or detector. Significant differences are discernible for some of the prominent sources vis-a-vis the absorption counts in figure 3. As expected, the Zr-plasma, Ag-plasma, Zr- $K\alpha$ , and the 20 keV images are nearly white, indicating total absorption and offering little contrast. But what is of prime interest is that the QX 65 keV Gaussian source and the MX 60 keV display marginally higher contrast than the conventional BX 120 kV x-rays. More particularly, the QX 65 keV appears to be the best source due to the increased flux arriving at the detector. The quasi-monochromaticity of such newly developed x-ray sources should therefore result in more reduced radiation fluxes than broadband devices (Achterhold *et al* 2013, Chen *et al* 2013, Powers *et al* 2014, Khrennikov *et al* 2015).

In order to investigate the dependence on the geometry of phantoms, we repeated the GEANT4 models using the spherical module in figure 2. In figure 5 we plot the calculated photon counts as for the rectangular phantom in figure 3, and find both sets of data to be



**Figure 3.** Rectangular phantom x-ray absorption: Counts of photons reaching the detector as a function of total input photons in simulations. The  $K_{\alpha}$  of Zr and Ag are respectively 15.7 keV and 22.0 keV. Relative statistical error in the counts at the detector was less than 0.1%.



**Figure 4.** Rectangular phantom x-ray imaging contrast: simulated x-ray image using data from the bar plot above in figure 3. Darker sections indicate more photons reached the detector while lighter sections indicate fewer incident photons reaching the detector, corresponding to air and bone layers respectively. The QX 65 keV Gaussian input spectrum shows the best contrast, comparable to or better than the conventional 120 KV BX spectrum.

consistent and similar. The increased flux through the spherical phantom compared to the rectangular phantom is likely due to varying thickness of the sphere while the rectangular phantom is uniform. Given the variety of x-ray distributions, that confirm the veracity of the comparisons although realistic situations may yet show greater variations. The relative independence on geometry is also reflected in the images through the spherical phantom

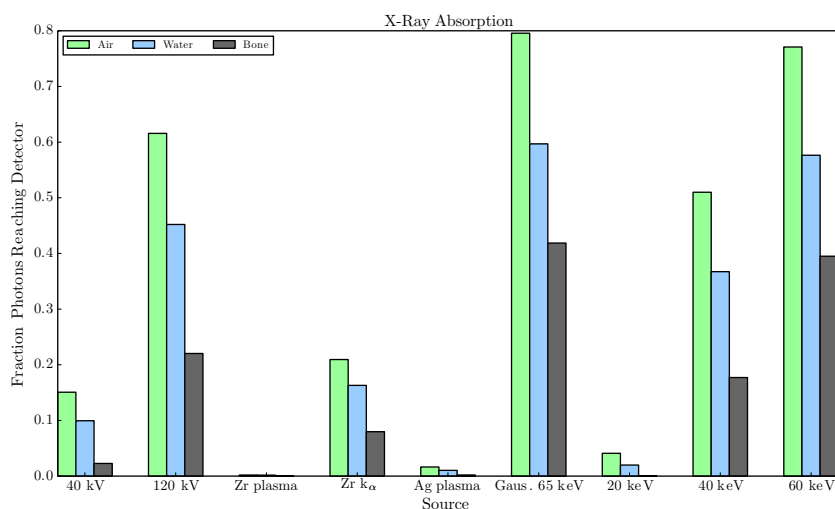


**Figure 5.** Spherical phantom x-ray absorption: counts of photons reaching the detector as a function of total input photons in simulations. The  $K\alpha$  of Zr and Ag are respectively 15.7 keV and 22.0 keV. Relative statistical error in the counts at the detector was less than 0.1%.

presented in figure 6. Again, the QX 65 keV is seen to have somewhat better contrast than the 120 kV while having higher penetration through the phantom. Figures 4 and 6 use different scales because the very low penetration of the lowest energy sources (Ag plasma, Zr plasma, and 20 keV) are pure white regardless of what penetration value is considered black. The gray value differences for the higher energy sources in figure 4 would be similar to the 40 keV source in figure 6 if the scales were the same. So the grayscales for each of these figures were selected in order to highlight contrast differences among the QX 65 keV, 120 kV, and 60 keV sources.

It is apparent from figures 3–6 using rectangular and spherical phantoms in figure 2 that the geometry of target significantly affects *relative* photon absorption counts and image quality.

#### 4.2. Quasi-monochromatic sources

The results presented in the previous section demonstrate the viability of QX sources around 65 keV for imaging, at least comparable to conventional BX sources. Increasing monochromaticity make those suitable not only for imaging but also for radiation therapy. That is because the x-rays are sufficiently energetic as to activate atomic features involving deep inner shells in high-Z species, up to the  $K$ -shell ionization edge and resonant  $K\alpha$  absorption. Figure 7 shows the  $K$ -edge and the  $K\alpha$  energies of tungsten and gold that are accessible owing to the width of the laser and accelerator driven inverse Compton x-ray source (Powers *et al* 2014). That could be of immense interest in biomedical applications since high-Z embedded nano-moieties of platinum or gold have been shown to have enhanced radiosensitization properties for increasing cell-killing using low energy keV x-rays, in comparison with conventional high energy MeV x-rays from linear accelerators (Lim *et al* 2015). In the next section we compare and contrast low and high energy BX sources, using a metric for determining the efficacy of two different x-ray flux distributions.

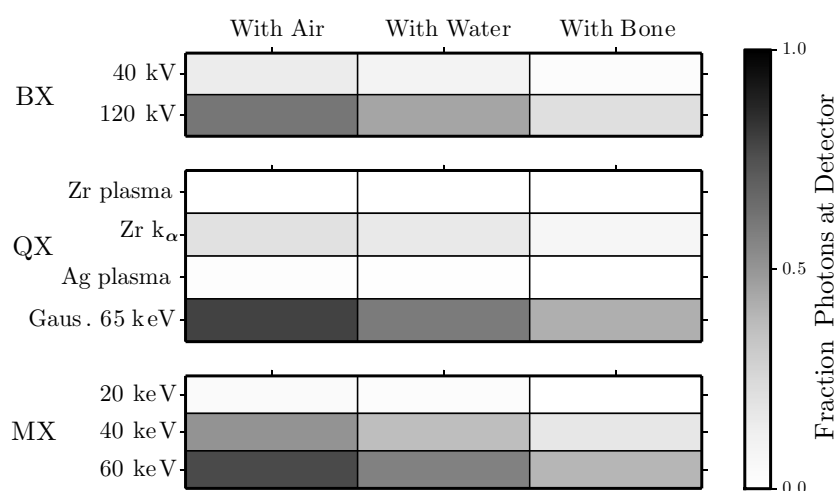


**Figure 6.** Spherical phantom x-ray image contrast: simulated x-ray image using data from the bar plot in figure 5. Darker sections indicate more photons reached the detector while lighter sections indicate fewer incident photons reaching the detector, corresponding to air and bone layers respectively. The QX 65 keV Gaussian input spectrum shows the best contrast, comparable to or better than for the conventional 120 KV BX spectrum. Results are similar to those in figure 4. The scale is adjusted from figure 4 in order to accommodate the different geometries of the phantoms and for improved clarity in the contrast.

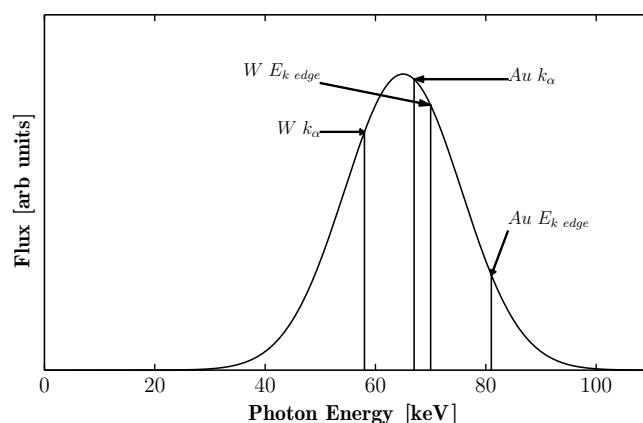


**Figure 7.** The laser-driven Compton QX source with Gaussian energy width and distribution (Powers *et al* 2014). Atomic  $K$ -shell features in tungsten ( $Z = 74$ ) and gold ( $Z = 79$ ) at  $\sim 65$  keV are shown; platinum ( $Z = 78$ ) energies is slightly lower than gold.  $E(K\text{-edge}) = 69, 78, 81$  keV for  $Z = 74, 78, 79$  and  $E(K\alpha) = 59, 67, 68$  keV respectively. Resonant  $K$ -shell processes in all these high- $Z$  elements may be activated for enhanced x-ray absorption (Pradhan *et al* 2009, Montenegro *et al* 2009, Nahar and Pradhan 2015).

#### 4.3. Metric for x-ray absorption efficiency: broadband sources

In section 2.2, we defined a metric to compute sensitizing efficiencies of any two x-ray sources, with the quantity  $\eta(V, V'; \rho_1, \rho_2)$ , where  $V$  and  $V'$  characterize the energy distributions and  $\rho_1, \rho_2$  the densities of targets high- $Z$  moieties. For example, for BX the spectral shapes of the

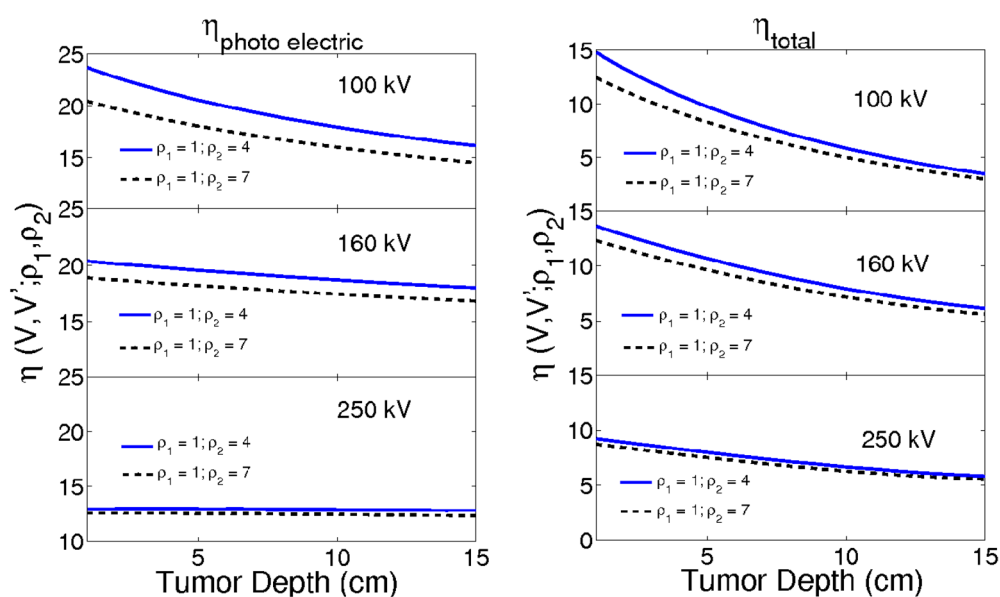


**Figure 8.** Radiosensitization ratios  $\eta_P$  (left) and  $\eta_{\text{Tot}}$  (right) (equation (5)) comparing the 100 kV, 160 kV and 250 kV sources relative to 6 MV irradiation of an Au-sensitized tumor layer as function of depth. As the Au-concentration increases from  $1 \text{ mg ml}^{-1}$  to  $4 \text{ mg ml}^{-1}$  and  $7 \text{ mg ml}^{-1}$ , the enhancements are between factors of 12–24 for the PE component that results in Auger-electron decays, and factors of 8–15 for the total.

bremsstrahlung broadband output are described by peak potentials  $V$  and  $V'$ . In an earlier work (Lim *et al* 2015) we studied attenuation of x-rays mediated by platinum in radiosensitizing agents such as carboplatin from 160 and 6 MV BX sources. It was shown that whereas the 6 MV BX spectral shape, such as employed in radiation therapy using LINACs, extends to high MeV energies needed for deep penetration, most of the interaction with a high- $Z$  sensitizing agent peaks in the low energy region  $E < 100 \text{ keV}$ , as determined by the dose enhancement factor which decreases by about a factor of two for  $E > 200 \text{ keV}$ . On the other hand, the low energy BX sources with accelerating potentials in the 100–200 kV range have most of their photon flux distribution also in the  $E < 100 \text{ keV}$  range.

In order to compare the sensitization efficiency for the low and high energy BX sources using the metric  $\eta$ , we divided the attenuation coefficients in two parts,  $\eta_P$  and  $\eta_{\text{Tot}}$ , the former due to photoexcitation of electrons and the latter referring to total attenuation including photon scattering. Using a  $\text{H}_2\text{O}$  phantom and Au-sensitizer, we carry out PHOTX calculations with an 1 cm Au layer embedded in the phantom at a depth of 10 cm, and concentrations  $\rho_1 \equiv \rho(\text{H}_2\text{O})$  and  $\rho_2 \equiv \rho(\text{Au})$  specified in the figures. In figure 8 we compare three low energy BX sources, 100 kV, 160 kV and 250 kV, relative to the high energy 6 MV, with respect to change in Au-concentration factor from  $1 \text{ mg ml}^{-1}$  to  $4 \text{ mg ml}^{-1}$ , or  $1 \text{ mg ml}^{-1}$  to  $7 \text{ mg ml}^{-1}$  of Au: $\text{H}_2\text{O}$  in the sensitized layer in the  $\text{H}_2\text{O}$  phantom. We find that the lower energy sources have absorption enhancements between factors of 12–24 for the PE component that results in Auger-electron decays, and factors of 8–15 for the total. From the point of view of potential applications this indicates that tumors embedded with gold will absorb much more energy from low energy than high energy x-ray sources compared to water alone.

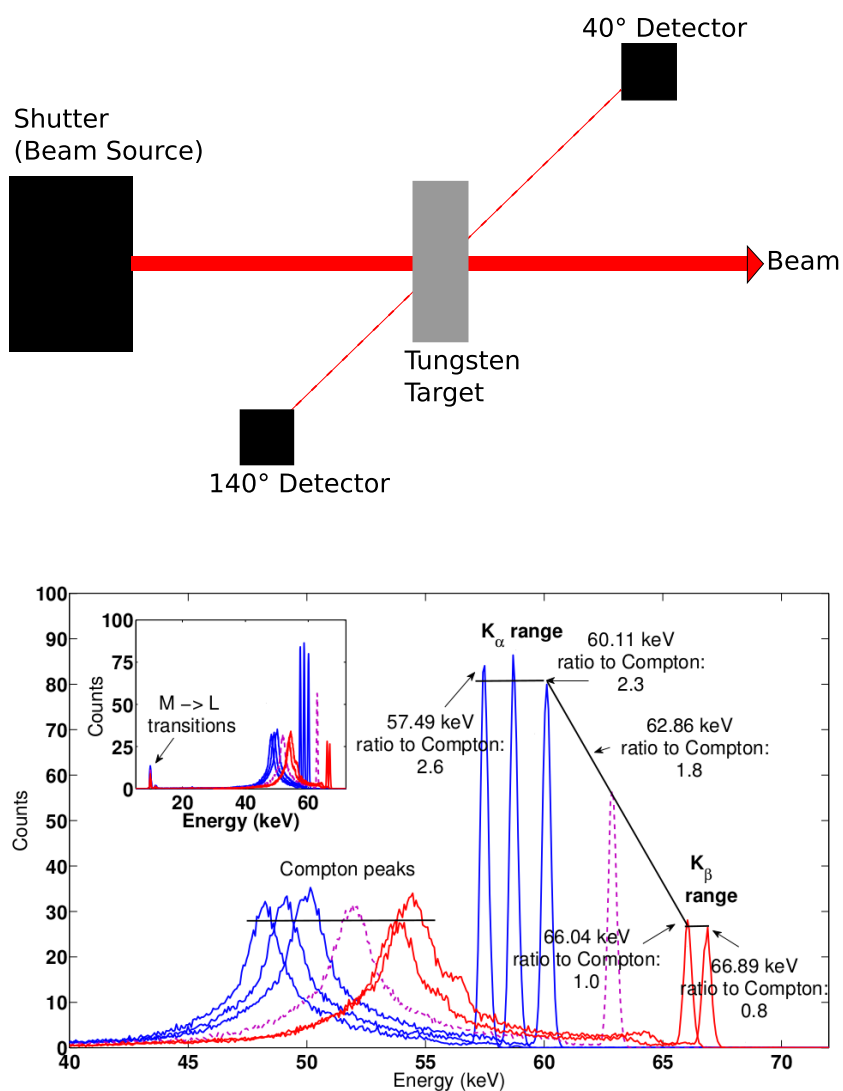


**Figure 9.** Experiments to detect  $K\alpha$  resonance fluorescence. The top panel shows the setup of the resonance experiments carried out at ESRF. Monochromatic beams were fired at a  $230\ \mu\text{m}$  tungsten target. Forward and backward scatter were detected at  $40^\circ$  and  $140^\circ$ , respectively. ESRF spectra (bottom) at energies close to the  $K\alpha$  and the  $K\beta$  complexes of tungsten. The blue lines correspond to  $E \sim K\alpha$  and the red lines to  $E \sim K\beta$ . The red-dashed line is at an energy intermediate between the  $K\alpha$  and  $K\beta$ . The broad Compton peaks and the  $M \rightarrow L$  complex are also measured.

#### 4.4. Synchrotron beam resonance scattering

The results of six separate measurements from the ESRF synchrotron are displayed in figure 9 for a tungsten target. The signature of  $K\alpha$  resonance fluorescence are predicted to manifest themselves in enhanced emission at or close to the  $K\alpha$  energy (Vinko *et al* 2012, Nahar and Pradhan 2015). The measured spectra correspond to scans across the tungsten  $E(K\alpha) \sim 59\ \text{keV}$  ( $K\alpha_1 = 59.32\ \text{keV}$ ,  $K\alpha_2 = 57.98\ \text{keV}$ ) and  $E(K\beta) \sim 67.24\ \text{keV}$ . In addition to the averaged

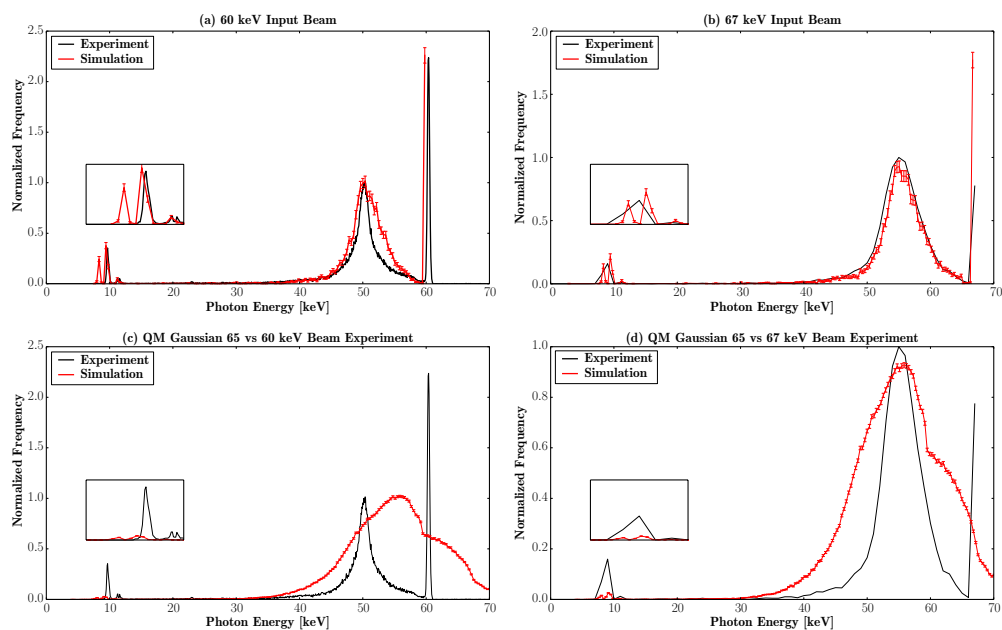


**Figure 10.** GEANT4 simulations of observed spectra from ESRF in figure 9 using a tungsten target and input MX energy beams at 60 keV (a) and 67 keV (b). The four main features are reproduced: the  $M \rightarrow L$  emission, broad Compton peak,  $K\alpha$  and  $K\beta$ . Panels (c) and (d) show GEANT4 simulations of the inverse Compton scattering source compared with experimental results for 60 keV and 67 keV MX energy beams, respectively. The same features are reproduced at reduced intensity. Error bars are the standard error on the mean, i.e. the standard deviation divided by the square root of the counts.

$K\alpha$  energy, the incident MX beams are tuned to energies slightly lower and higher than the  $K\alpha$  at 57.49 and 60.11 keV. Similarly, two energies close to  $E(K\beta)$  are chosen, 66.04 and 66.89 keV. In order to study the variation and the decrease in intensity from the  $K\alpha$  and  $K\beta$ , an intermediate energy is also chosen at 66.04 keV. The broad Compton peaks and the  $K\alpha$ ,  $K\beta$  emission lines are observed in the scattered spectra, and their relative intensities may be inferred from respective photon counts. The ratios of the individual  $K\alpha$  and  $K\beta$  lines relative to the Compton peak are also marked in figure 9. We consider only the results at backscatter angle of  $140^\circ$ , since the scattering in the forward direction at  $40^\circ$  is dominated by the background and measured intensities are less reliable. The observed spectra also show the  $M \rightarrow L$  emission flux, that is much smaller than the  $K\alpha$  complex.

GEANT4 simulations of spectral intensities corresponding to figures 9 are shown in 10. Although we are able to fit the positions and heights well, the detailed shapes appear to be significantly narrower than observed, which also implies lower computed fluxes. Emission from the,  $M \rightarrow L$  complex of lines, due to Auger decays filling up the  $L$ -shell following  $K$ -shell ionization, is not well modelled by GEANT4 and the energies are significantly different from observed ones.

In addition, we carried out similar simulations using the inverse Compton scattering source modelled as a Gaussian, shown in figures 10(c) and (d). These simulations are intended to demonstrate that a QX source covers the necessary range at the appropriate energies to active resonant  $K$ -shell processes for enhanced x-ray absorption as detailed in figure 7 (Pradhan *et al* 2009, Montenegro *et al* 2009, Nahar and Pradhan 2015).

While there is overall qualitative agreement between the GEANT4 simulations and the prominent and characteristic x-ray features, there is no clear signature, and further experimental and numerical studies are needed in order to ascertain the presence of  $K\alpha$  resonance fluorescence. The observed features in figure 10 are basically what is expected from elastic Rayleigh-type scattering, and the  $K\alpha$  intensity variations, if present at the synchrotron beam intensities, are subsumed therein. These results are preliminary, though illustrative of underlying physical features and processes in x-ray spectral formation. Additional experimental study is needed including angular dependence in the forward and backward scattering directions, even though both involve problems of isolating the signal from the background. In addition, more detailed atomic rates for the multitude of Auger transitions are also required in GEANT4 in order to fully model the emission complexes of lines due to  $K\alpha$ ,  $K\beta$  and the  $L$ -complexes from  $M \rightarrow L$  transitions. However, given the significance of the quantum effects it would be highly worthwhile to pursue these investigations.

## 5. Conclusion

A comparative theoretical and experimental study of a variety of conventional and emerging x-ray sources leads to following conclusions.

1. Whereas broadband sources lack energy specificity, new quasi-monochromatic and monochromatic sources may be more efficient in interrogating and activating sensitizing moieties for imaging and therapy.
2. In contrast to laser driven inverse Compton x-ray sources (figure 1(f)), the high-intensity laser produced sources yield x-ray output with a large BX component at low energies (figures 1(c)–(e)), and are therefore not at present suitable for imaging or other biomedical applications. The former type of QX source with most output centered at  $\sim 65$  keV display image contrast better than the broadband 120 KV generally employed for radiography. Optimization of such newly developed QX sources based on laser driven inverse Compton scattering offer the possibility of lower radiation dose than current BX sources. We further note that the QX Gaussian output around 65 keV is sufficient to excite-ionize the  $K$ -shell of high- $Z$  nanomoieties dominated by Pt or Au, commonly considered for radiotherapy.
3. The absorption metric  $\eta$  outlined in sections 2.2, 3.3, and 4.3 indicates that the efficacy of low energy KV broadband sources relative to high energy MV sources could be up to an order of magnitude or more higher when coupled with a high- $Z$  sensitizer, such as gold.
4. We investigated experimentally and theoretically, as illustrated in figures 7, 9, and 10, whether the new QX and established synchrotron MX sources might be capable of demonstrating enhancement of  $K$ -shell x-ray absorption via  $K\alpha$  resonance fluorescence and accelerated Auger processes involving higher electronic shells and transitions. There was no discernible signature found, and it is likely that significantly higher intensities such as in the x-ray free-electron laser (*viz.* Vinko *et al* (2012)) are required to observe induced fluorescence. That is the reason we have theoretically proposed, and plan further Geant4 simulations, for twin-beam x-ray beam resonantly tuned excitations at the  $K\alpha$  and  $K$ -edge energies, which might accelerate the process at much lower intensities (Nahar and Pradhan 2015).

More extensive numerical simulations and experiments on each of these conclusions are needed to potential translation to realistic imaging and therapy under clinical conditions.

## Acknowledgments

The computational work was carried out at the Ohio Supercomputer Center in Columbus Ohio.

## References

- Achterhold K, Bech M, Schleede S, Potdevin G, Ruth R, Lowen R and Pfeiffer F 2013 Monochromatic computed tomography with a compact laser-driven x-ray source *Sci. Rep.* **1313** 1–4
- Agostinelli S *et al* 2003 Geant4—a simulation toolkit *Nucl. Instrum. Methods Phys. Res. A* **506** 250–303
- Allison J *et al* 2006 Geant4 developments and applications *IEEE Trans. Nucl. Sci.* **53** 270–8
- Allison J *et al* 2016 Recent developments in Geant4 *Nucl. Instrum. Methods Phys. Res. A* **835** 186–225
- Baldelli P, Taibi A, Tuffanelli A and Gambaccini M 2003 Quasi-monochromatic x-rays for diagnostic radiology *Phys. Med. Biol.* **48** 3653–65
- Banerjee S *et al* 2015 Compact source of narrowband and tunable x-rays for radiography *Nucl. Instrum. Methods Phys. Res. B* **350** 106–11
- Birch I P, Kotre C J and Padgett R 2006 Trends in image quality in high magnification digital specimen cabinet radiography *Br. J. Radiol.* **79** 239–43
- Chen S *et al* 2013 MeV-energy x rays from inverse Compton scattering with laser-Wakefield accelerated electrons *Phys. Rev. Lett.* **110** 155003
- Cho S 2005 Estimation of tumour dose enhancement due to gold nanoparticles during typical radiation treatments: a preliminary Monte Carlo study *Phys. Med. Biol.* **50** N163–73
- Hoheisel M, Lawaczeck R, Pietsch H and Arkadiev V 2005 Advantages of monochromatic x-rays for imaging *Proc. SPIE* 5745 1087–95
- Khrennikov K, Wenz J, Buck A, Xu J, Heigoldt M, Veisz L and Karsch S 2015 Tunable all-optical quasimonochromatic Thomson x-ray source in the nonlinear regime *Phys. Rev. Lett.* **114** 1950031–5
- Lakshmanan M N, Harrawood B P, Rusev G, Agasthya G A and Kapadia A J 2014 Simulations of nuclear resonance fluorescence in GEANT4 *Nucl. Instrum. Methods Phys. Res. A* **763** 89–96
- Le Sech C, Takakura K, Saint-Marc C, Frohlich H, Charlier M, Usami N and Kobayashi K 2000 Strand break induction by photoabsorption in DNA-bound molecules *Radiat. Res.* **153** 454–8
- Leung M K K, Chow J C L, Chithrani B D, Lee M J G, Oms B and Jaffray D A 2011 Irradiation of gold nanoparticles by x-rays: Monte Carlo simulation of dose enhancements and the spatial properties of the secondary electrons production *Med. Phys.* **38** 624–31
- Lim S *et al* 2015 Tumoicidal activity of low-energy 160 KV versus 6 MV x-rays against platinum-sensitized F98 glioma cells *J. Radiat. Res.* **56** 77–89
- Montenegro M, Nahar S N, Pradhan A K, Huang K and Yu Y 2009 Monte Carlo simulations and atomic calculations for Auger processes in biomedical nanotheranostics *J. Phys. Chem. A* **113** 12364–9
- Nahar S N and Pradhan A K 2015  $K\alpha$  resonance fluorescence in Al, Ti, Cu and potential applications for x-ray sources *JQSRT* **155** 32–48
- Nahar S N, Pradhan A K and Lim S 2011  $K\alpha$  transition probabilities for platinum and uranium ions for possible x-ray biomedical applications *Can. J. Phys.* **89** 483–94
- Powers N D, Ghebregziabher I, Golovin G, Liu C, Chen S, Banerjee S, Zhang J and Umstadter D P 2014 Quasi-monoenergetic and tunable x-rays from a laser-driven Compton light source *Nat. Photon.* **8** 28–31
- Pradhan A K, Nahar S N, Montenegro M, Yu Y, Zhang H L, Sur C, Mrozik M and Pitzer R M 2009 Resonant x-ray enhancement of the Auger effect in high-Z atoms, molecules, and nanoparticles: potential biomedical applications *J. Phys. Chem. A* **113** 12356–63

- Redus R H, Huber A, Pantazis J, Pantazis T and Sperry D 2006 Design and performance of the X-123 compact x-ray and gamma-ray spectroscopy system *IEEE Nuclear Science Symp. Conf. Record* [R15-4](#)
- Storm M *et al* 2014  $K\alpha$  x-ray imaging of laser-irradiated, limited-mass zirconium foils *Phys. Plasmas* [27 072704](#)
- Vinko S M, Ciricosta O and Cho B I 2012 Creation and diagnosis of solid density plasma with an x-ray free-electron laser *Nature* [482 59-U75](#)